Chapter 22
Surface-Modified Lanthanide Nanomaterials for Drug Delivery

Nitya R. Chawda, S. K. Mahapatra, and I. Banerjee

Abstract The chapter highlights the importance and possibility of detrimental effects of lanthanide-based nanomaterials, surface capping, and toxicity. Lanthanide-based nanomaterials serve multimodality approach such as diagnosis and therapy. This speciality makes them superior over their other counterparts like transition metals and organic-based materials. The loose ions leached from the contrast agent used for magnetic resonance imaging (MRI) causes possibility of nephrotoxicity leading to nephrogenic systemic fibrosis (NSF). It also indulges the readers to understand synthesis mechanism for elongated mixed-phase rare-earth oxides and hydroxide nanostructures. The basic principle of transition and crystallization temperatures required for rare-earth-based oxide formation is specially highlighted and explained in detail using X-ray diffractometer (XRD), thermogravimetric analyzer (TGA), differential scanning calorimetry (DSC), and Fourier-transform infrared spectroscopy (FTIR) data. Furthermore, the lanthanide nanorods have been employed as contrast agent in MRI and drug delivery studies. The promising results like longitudinal proton relaxivity (r_1) value of 13.3 mM^{-1} s^{-1} and drug-loading capacity of 5-flurouracil are ~28% for FA-capped Gd_2O_3 nanorods in comparison to bare sample (~9%) that is best endowed to its unique structure and skillful capping. These advantages of well-capped FA-Gd_2O_3 nanorods are promising candidates for simultaneous bioimaging and drug delivery system due to the presence of FA over its surface. It will server further as potentially equipped candidate for clinical applications for targeted diagnosis and therapy which in combination is to be known as theranostics.

Keywords Drug delivery · Paramagnetic · Contrast agent · Nanomaterials Magnetic resonance imaging (MRI)

N. R. Chawda · I. Banerjee (✉)
School of Nano Sciences, Central University of Gujarat, Gandhi Nagar, Gujarat, India
e-mail: indrani.banerjee@cug.ac.in

S. K. Mahapatra
Department of Physical Sciences, Central University of Punjab, Bhatinda, Punjab, India

1 Introduction

Nanotechnology has found enormous importance in biomedical sciences toward effective diagnosis, therapy, and elimination of diseases. The advancement of science and technology has developed the need for multitasking and multifunctional systems which can replace older, costlier, and time- and resource-consuming conventional systems and methods [1]. As per the American Cancer Society's estimation of 2017, around 1650 people die every day in the worlds most advanced country of United States due to cancer [2]. Owing to such a fatal threat, continuous as well as considerable efforts are made for expanding nanomaterials as next-generation promise for biomedical medicines and drug delivery systems. Nanomaterials possessing multimodality such as diagnosis and therapy, like imaging and targeted drug delivery, could certainly fulfil a promise and would reduce other side effects [3]. It is also essential to design such systems in order to enhance targeting strategies and improve biodistribution, enhanced blood circulation, and penetration depth of existing body barriers, and to reduce required volume needed for distribution [4]. Therefore, nanomaterials (NMs) which could response to light and magnet can contribute largely to diagnostics and image-guided drug delivery. However, most of the NMs designed for drug delivery lack optical properties (e.g., fluorescence and photothermal response) and magnetic properties of gadolinium-based lanthanides (paramagnetic property) as contrast agents used for magnetic resonance imaging (MRI). In this context, luminescence and magnetic properties of lanthanide materials are superior and useful over traditional quantum dots, green fluorescent proteins, and organic dyes [5].

Lanthanides also referred as "rare-earth" elements ranging from lanthanum (57) to lutetium (71) are widely utilized in cancer diagnosis (imaging) and drug delivery (therapy) [6–8]. The Ln^{3+} ions possess redox stability which makes them suitable for cellular applications with the additional benefit from their luminescent properties ascribed to 4f–5d charge transfer and f–f transitions [9]. Lanthanide-based nanomaterials (Ln-NMs) have one of the most outstanding properties of upconversion [6, 10]. The process is related to the nonlinear anti-stocks process, by which it can effectively convert either two or more low-energy continuous near-infrared (NIR) photons into high-energy photons, when embedded in suitable inorganic host matrix [11]. The main reason for rapid demand of upconversion nanoparticles (UCNPs) for biomedical purposes is its excitation wavelength (e.g., 980 nm) which falls under "optical transparency window" (700–1100 nm) [6]. It also supports for various advantages such as no photodamage to living organisms, low autofluorescence background, high signal-to-noise ratio, detection sensitivity, and high penetration depth in animal tissues [12, 13]. The UCNPs are superior to other NMs due to their chemical stability, photostability which is also free of on-off blinking, measurable single-particle excitation [14], multi-color emission (i.e., red, green, blue), multimodal imaging (i.e., positron emission tomography (PET), magnetic resonance imaging (MRI) [15], and upconversion luminescence (UCL)) [16] and would

also help for photo-triggered drug delivery [17, 18]. Surface-modified lanthanide-based nanomaterials used for drug delivery can act as excellent imaging probe to locate cancer site as well as act as efficient carrier for targeting site with therapeutic agents [19, 20]. Such a multimodal Ln-NMs are ideal to clarify pharmacokinetics and pharmacodynamics by additionally providing rational support for decisions of individual patients [21].

The model drug used in the present study is 5-fluorouracil (5-FU). It is an acidic water soluble drug along with antineoplastic agent. It is one of the most commonly used chemotherapeutic compounds for various tumors such as breast, colorectal, gastric, pancreatic, ovarian, head, and neck cancer [22, 23]. Apart from its various applications, it is an antimetabolite of pyrimidine analogue and is used to inhibit synthesis of DNA and RNA during the S-phase of the cell cycle. Some of the limitations of 5-FU are short biological half-life due to rapid metabolism and nonselective action against healthy cells [24]. Therefore, it is significant to design target-specific nanocarrier to the cancerous cells with sustained release so as to minimize side effects to nearby healthy cells [25].

The present chapter explains the formation mechanism of FA-capped Gd_2O_3 nanorods for its bimodal application. The FA-capped Gd_2O_3 nanorods are used for bimodal application as contrast agent for MRI bioimaging and FA-capped Gd_2O_3 nanorods-5-FU system for drug delivery. The FA-Gd_2O_3 was synthesized by coprecipitation method using FA as capping and stabilizing agent. The FA was chosen due to its biocompatibility, site specificity, fluorescence property, antitumor effect, and G-quartet-forming property [26]. It binds with folate receptors, which are widely found in most cancer cells [27], and it is interesting to note that the folate receptor density increases at the advanced stage of cancer [28]. The selected model drug 5-FU is very less explored with gadolinium oxide nanocarriers; one of the report by Zhang et al. showed results of 5-FU loaded with nanosheets of Gd_2O_3 and Sm_2O_3 for drug delivery applications. The nanosheets being bare nanocarriers could not have provided them with efficient loading, and the pH-triggered release showed maximum release within 24 h [29]. In the present study, the capping agent itself acts as growth modulator for anisotropic growth of nanoparticle, stabilizing them for longer time and improving the dispersity in aqueous solvent with respect to time. It enhances biocompatibility and acts as fluorescent probe for tracking and diagnosis. The restricted core particle being paramagnetic in nature is used for MRI studies and reduces toxicity inhibiting release of Gd^{3+} ions by formation of stable capping over the surface of oxide nanorods. The oxides with low solubility product having higher stability that chelated complexes, hence compared to commercially available Gd^{3+}-chelated compounds like Magnevist [30–36] oxides of gadolinium helps in reducing toxicity due to leaching of free Gd^{3+} ions. The compatibility and morphology add to the multifunctional activity of the present system. The FA-capped Gd_2O_3 nanorods were employed for bioimaging as contrast agent for in vitro MRI studies and were also effectively used for loading and release of 5-FU in simulated physiological medium of PBS having pH 7.4 at 37 °C.

2 Surface Functionalization of Nanomaterials

Surface tailoring of nanomaterials is a challenging and most significant task for desired applications of synthesized nanomaterials. The clinical applicability of NMs depends on suitable surface functionalization or modification, while the change in different properties and their extent of effects also depends on choice of ligands or molecules. Surface coatings of NMs are attained with two different modes either in situ (along with nucleation, while formation of NMs) or ex situ (post-synthesis, after NMs are obtained). The procedure of linking surface molecules is carried out either through end-grafting (anchored through one end of the single molecule, e.g., PEG and PLGA-PEO) or surface encapsulation (through multiple connections carrying multiple active groups, e.g., silica) [37]. The properties like stability, biocompatibility (toxicity), magnetization, relaxivity, optical emission, and contrast ability are purely dependent on efficiency and mode of capping materials with the suitable selection of ligands. For example, Cho Rong Kim and co-workers investigate longitudinal (r_1) and transverse (r_2) water–proton relaxivities of ultrasmall gadolinium oxide (Gd_2O_3) nanoparticles by varying surface-coating ligand size and found that both r_1 and r_2 values decreased with increasing ligand size [38]. Tamilmani Vairapperumal et al. reported catechin-capped gadolinium-doped $LaVO_4$ nanoparticles which showed increase of saturation magnetization from paramagnetic to superparamagnetic due to capping [39]. Tirusew Tegafaw et al. have investigated ligand-chain effects of hydrophilicity on the relaxometric properties of ultrasmall Gd_2O_3 nanoparticles [40]. These are various factors of the surface modification that play crucial role in its functionality like colloidal stability, biocompatibility, and role of functionalized moieties or ligands for fulfilling selective, targeting, and specific interactions for enhancing applicability of NMs for multimodality. Therefore synthesis of monodispersed, biocompatible surface-functionalized nanoparticles is of utmost importance for biomedical applications [34, 41].

The surface functionalization induces imaging, detection, therapeutic, and targeted capabilities to NMs. The multi-functionalities of nanomedicine lie in simultaneous detection, diagnosis, and treatment along with deep tissue penetration, enhanced contrast, specific targeting, and externally triggered drug delivery [42]. These applications are only possible if surfaces are tailored with specific surface molecules.

3 Materials and Methods

3.1 Materials

Gadolinium nitrate hexahydrate ($Gd(NO_3)_3 \cdot 6H_2O$) and 5-flurouracil (5-FU) were purchased from Sigma-Aldrich of purity 99.9% and ≥99%, respectively; sodium hydroxide (NaOH) and hydrogen peroxide (30% W/V) were procured from

S.D. Fine Chem. Ltd., Mumbai, India. Nitric acid was purchased from Molychem (India) Ltd., folic acid was purchased from HiMedia chemicals India, and urea was purchased from Rankem (Delhi India). All the chemicals were used without further purification.

3.2 Synthesis of Folic Acid (FA)-Capped Gadolinium Oxide Nanorods (Gd$_2$O$_3$·NRs)

The folic acid (FA)-capped gadolinium oxide (Gd$_2$O$_3$) nanorods were synthesized using co-precipitation method at ~100 °C. At room temperature, aqueous solutions of NaOH was added to aqueous solution of Gd(NO$_3$)$_3$ dropwise at the rate of 60 μL min^{-1} with stirring speed of 900 rpm. The resultant white powder of Gd(OH)$_3$ was obtained via first step of synthesis. In the second step, urea and H$_2$O$_2$ were mixed to form an adduct solution which controls the release of oxygen from H$_2$O$_2$ as required for oxidation of Gd(OH)$_3$ to Gd$_2$O$_3$ where FA was used as capping agent. In first step, 25 mL of 175 mM aqueous NaOH was added dropwise to 25 mL of 58 mM aqueous Gd(NO$_3$)$_3$ at the rate of 60 μL min^{-1} with stirring speed of 500 rpm. The resulting solution turned to turbid milky white suspension. After the completion of reaction, the mixture was centrifuged at 6000 rpm with repeated wash using chilled water to neutralize the pH and then dried to get Gd(OH)$_3$. Gd(OH)$_3$ was weighed according to stoichiometry and transferred to a 250 mL round-bottom flask followed by addition of 20 mL of water with stirring speed of 750 rpm until dispersed. Another solution containing 100 mg FA, 100 mg urea, and 30 mL of 30% H$_2$O$_2$ was added to the previous solution at the rate of 700 μL min^{-1} with 750 rpm stirring speed. The complete mixture of dispersed solution was then refluxed at 100 °C for 48 h at 2000 rpm on adding 10 mL 30% H$_2$O$_2$ after every 12 h of interval to get FA-Gd$_2$O$_3$. The pH was measured after adding each solution to the reaction mixture which was alkaline (~pH 9–10) which is preferred for elongated structures as reported in literatures [43, 44]. The FA controlled the growth uniformity at a preferred direction. The carboxyl functionality of FA structure interacts with the charge density of available surface which the gadolinium hydroxide gets converted to a gadolinium oxide. The resulting FA-Gd$_2$O$_3$ was centrifuged at 8000 rpm to remove the unreacted urea and FA with repeated washing using water and ethanol. The bulky structure of FA does not allow other ions involved in nucleation and ripening to come in vicinity once FA is attached over the surface. This growth formulation helps in proceeding along a single-oriented direction (Scheme 22.1). Other conditions of temperature, pH, and concentration of Gd^{3+} ions also contribute to it. The obtained sample was dried in vacuum oven at 50 °C for 12 h and stored for further characterizations. The Milli-Q water (Millipore SAS 67/20 Mosheim) of 10^{-7} S cm^{-1} was used throughout.
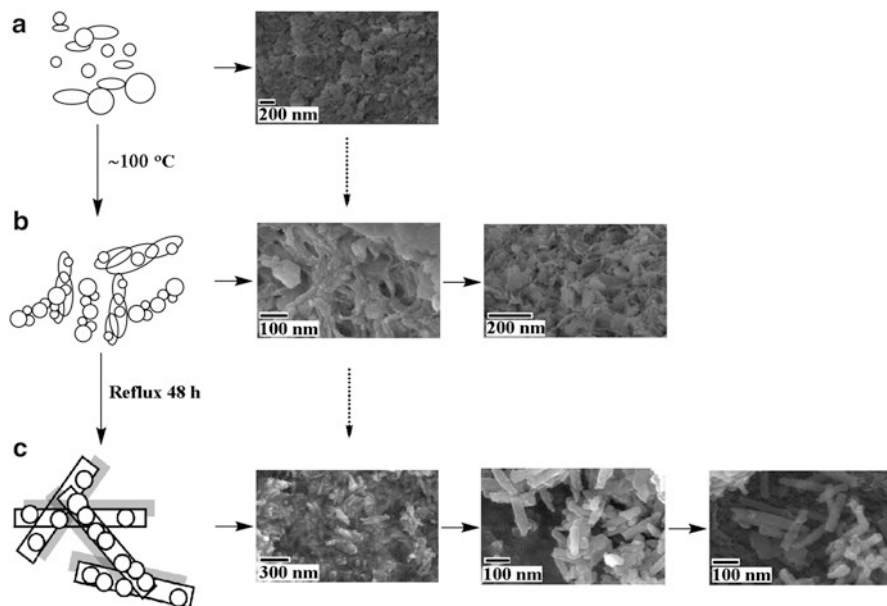
Scheme 22.1 (**a**) Random flakes of Gd_2O_3, (**b**) Flakes of Gd_2O_3 attached to form nanorods and (**c**) Complete growth of Gd_2O_3 nanorods

3.3 Characterization of Folic Acid (FA)-Capped Gadolinium Oxide Nanorods ($Gd_2O_3 \cdot NRs$)

To study the morphology of FA-Gd_2O_3, field-emission scanning electron microscopy (FESEM) QUANTA 200 FEG from FEI Netherlands was used. The X-ray diffractometer (XRD) pattern of FA-GdNRs was performed on PANalytical *X'Pert Pro* instrument of Cu-Kα wavelength ($\lambda = 1.54$ Å). The samples were scanned over a 2θ range of 10–80° with a step size of 0.013°. UV-Visible spectrophotometer (UV-1800 Shimadzu) was used for primary capping analysis. The FTIR spectra were recorded with PerkinElmer Spectrum 65 series of FTIR spectrophotometer. For FTIR, 1.5–2.5 mg of the sample was mixed with 185 mg KBr (AR, Sigma USA) for making pellets in press machine (model Mp-15) at 3–6 kg/cm^2 for 2–5 min. After a background scan with KBr pallet, the samples were analyzed at 4000–400 cm^{-1}. The TG-DSC analysis for all the samples was recorded using TG-DSC-Mettler-Toledo Star-3 system in a platinum crucible under inert N_2 atmosphere at 10 K min^{-1} and temperature range from room temperature to 1000 °C.

Surface capping with folic acid was investigated by FTIR spectra using KBr pallet at 4000–400 cm^{-1} to find the peak shifting by comparative study of pure capping agent, bare sample without FA and FA-Gd_2O_3. The thermogravimetric analyzer TGA curve recorded from 45 °C to 1000 °C in inert condition of nitrogen with airflow over powder samples was used to estimate the amount of capping by mass loss.

3.4 Determination of Free Gd³⁺ Ions by Xylenol Orange and UV-Visible Spectrophotometry

Two millilitre of 0.1 mM of xylenol orange solution in acetate buffer (pH 5.88) was added to 50 μL of supernatant of bare-Gd_2O_3 and FA-Gd_2O_3 dispersant (1 mg mL⁻¹). The mixture was placed for UV-visible (350–650 nm). The amount of ions was calculated from fitted equation of absorbance ratio (λ_{max} = 578 and 437.5 nm) using calibration curve. The UV-1800 Shimadzu spectrophotometer was used for entire study at 298.15 K with an average of three scans.

3.5 The Gd³⁺ Ions Leaching Studies from Nanorods by Inductive Coupled Plasma-Optical Emission Spectroscopy (ICP-OES)

The sample preparation of FA-Gd_2O_3 was carried out by acid digestion method using nitric acid (i.e., HNO_3 70%) with heating over open flame till the clear and transparent solution was obtained. All the samples were later dissolved in ~2.0% HNO_3 for further detection using a Perkin Elmer ICP-OES.

4 Results and Discussion

4.1 Powdered X-Ray Diffractometer Analysis

Figure 22.1 illustrates powdered X-ray diffraction spectra of the samples. The XRD spectra showed mixture of amorphous and crystalline phase as no clear or perfect sharp peak was found. The diffraction spectra of as-prepared product could not be fitted to simple gadolinium hydroxide or oxide in ICDD or JCPDS database. The crystalline temperature for Gd_2O_3 was determined to be above 560 °C from TGA analysis presented in the following section. However, the as-synthesized sample was calcinated at 400 °C, so complete transition from hexagonal $Gd(OH)_3$ to cubic Gd_2O_3 was not achieved, and the sample showed mixed phases of hydroxides and oxides of gadolinium. The characteristic peaks corresponding to the mixed phases of hydroxide and oxide have been represented by asterisk (*) and octothorp (#), respectively, in the XRD spectra. The planes corresponding to (100), (110), (101), (200), (111), (201), (210), (300), (211), (102), (112), (310), and (131) represent the hexagonal phase of $Gd(OH)_3$ according to JCPDS card No. 83-2037. The planes corresponding to (211), (222), (400), (440), and (622) indicates formation of cubic Gd_2O_3 according to JCPDS card No. 43-1014. The XRD pattern of as-prepared FA-Gd_2O_3 presents three distinctive peaks at 28.1° corresponding to (110) and at
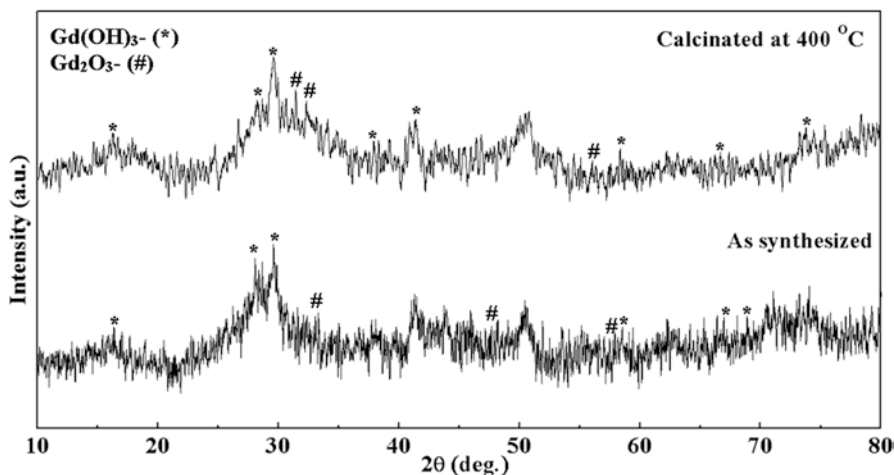
Fig. 22.1 XRD patterns of as-synthesized folic acid-capped-gadolinium oxide (FA-Gd$_2$O$_3$) and calcinated at 400 °C folic acid-capped-gadolinium oxide (FA-Gd$_2$O$_3$)

29.5° corresponding to (101) of Gd(OH)$_3$, respectively, and at 28.7° corresponding to (222) of Gd$_2$O$_3$ which are also indexed in XRD pattern of annealed samples at 400 °C. The intermediate phase of GdOOH planes indexed to (112) and (310) are also obtained supporting the phase transition observed in TGA analysis. The broad peaks are indicative of small crystallite size [45, 46]. The microstrain (ε) and average crystallite size (d) were calculated from Williamson-Hall (W-H) expression also known as Uniform Deformation Model (UDM):

$$\beta \cos\theta = \frac{0.9\lambda}{d} + 4\varepsilon \sin\theta \qquad (22.1)$$

where "β" is full width at half maximum abbreviated as (FWHM) of the diffraction peaks in radian, "θ" is the Bragg diffraction angle in radian, "λ" is the wavelength of Cu-Kα X-rays used having value of 0.154 nm, "d" is the crystallite size along the specified direction, and "ε" is microstrain associated with nanorods. Equation 22.1 gives straight line equation when plotted for $\beta \cos\theta$ versus $\sin\theta$. The slope gives the microstrain (ε), and its intercept (0.9λ/d) gives the crystallite size "d." The obtained microstrain for as-prepared sample is ~17.4 × 10^{-3}, and annealed sample at 400 °C possessed negative microstrain of ~7.8 × 10^{-3} which are in agreement with the earlier reports [47]. The negative microstrain after annealing is due to the relaxed state of nanocrystallites present in the nanorods. The decrease in microstrain on heat treatment is attributed to the closing of the pores and reduction of defects. The average crystallite sizes (d) estimated for the as-prepared and annealed samples were 33 nm and 3.4 nm, respectively. The decrease in the crystallite size on annealing is due to the coalescence or aggregation of the nanocrystallites by higher-thermal energy reducing the surface-free energy and providing driving forces for growth of

the crystals. The microstrain and crystallite size determination derived from the Uniform Deformation Model (UDM) showed that the microstrain is inversely proportional to the crystallite size on application of heat treatment which is in agreement with the reported data [47].

4.2   Field-Emission Scanning Electron Microscopy (FESEM) Imaging

Figure 22.2a shows FESEM image of synthesized samples of FA-Gd system. The Schematic 22.1 gives the insight of the growth mechanism and stepwise evolution of the nanorods via oriented grain attachment mechanism from the nanoparticle seeds followed by the formation of nanoflakes. The particle seeds and flakes start nucleating and growing along a preferred direction which is governed by the capping agents along with the pH and time of the reaction mixture. The nanorods generated at the final stage of synthesis and calcined were ~200 nm in length and ~20 nm in diameter. It could be speculated that the particles get attached via oriented attachment mechanism [48]. The micrograph clearly illustrates formation of particles at initial stage followed by coalescence and growth along a preferred direction through surface effects resulting in elongated shapes once common boundaries

Fig. 22.2 FESEM image of folic acid-capped-gadolinium oxide (FA-Gd$_2$O$_3$) nanorods. (**a**) Image showed particle attachment for elongated structure. (**b**) The formation and well-defined size of nanorods at low magnification
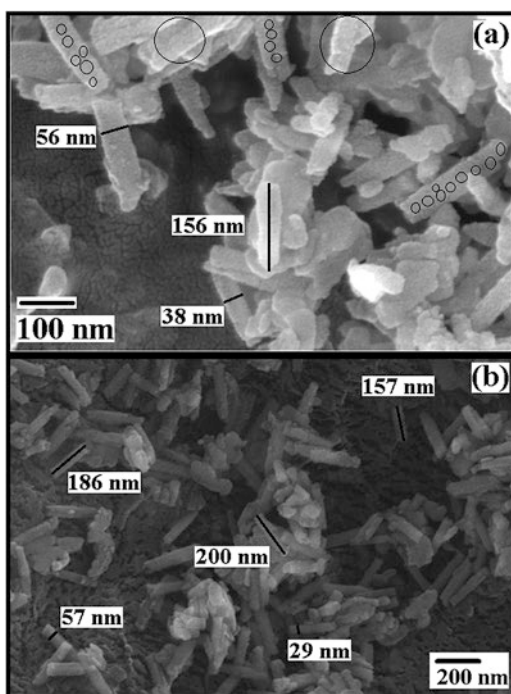
get eliminated. The factors like dipole–dipole interaction, perfect lattice match, and vanishing of adjoining interface between the particles act as the driving force for such unidirectional surface growth [48]. The capping agent present in reaction mixture also assists dipole–dipole interaction. The functional part of folic acid known as glutamate is attached to the Gd_2O_3 surface via carboxylate ($–COO^-$) functionality. The synthesis procedure involves reaction mixture to be continuously stirred which makes ions involving in Brownian motion which tend the particles to colloid and assist for their coalescence and growth in elongated direction through common crystallographic orientation. It is anticipated that reaction time and choice of suitable capping agent could assist in growth of nanoparticles in such organized manner.

4.3   Thermogravimetric Analysis

The significance of surface tailoring has already been discussed, and, therefore, surface capping was estimated by simultaneous TGA-DSC analysis of the as-synthesized sample. The average weight loss is predicted from the TGA curves given in Fig. 22.3. The plot explains four distinct weight loss phenomena depicting the transformation of gadolinium hydroxide to cubic gadolinium oxide crystallizing above 560 °C. The initial mass loss of 1.1 mg till 100 °C is attributed to the surface dehydration of the FA-capped sample. A loss of 1.82 mg till 260 °C is accounted for the melting of surface capping of folic acid whose melting point is 250 °C. Therefore, the estimated capping amount was 1.82 mg which is 0.05 mg mg^{-1} of FA-Gd_2O_3. This weight loss is followed by a loss of 2.84 mg till 400 °C attributed to the phase transition of $Gd(OH)_3$ to intermediate phase of GdOOH in the form of $Gd(OH)_3 \rightarrow GdOOH + H_2O$ for which corresponding endothermic peak in DSC plot is at 337 °C (Fig. 22.4). The final weight loss of 3.97 mg is observed for the second step of dehydration in the form of $2GdOOH \rightarrow Gd_2O_3 + H_2O$ for which
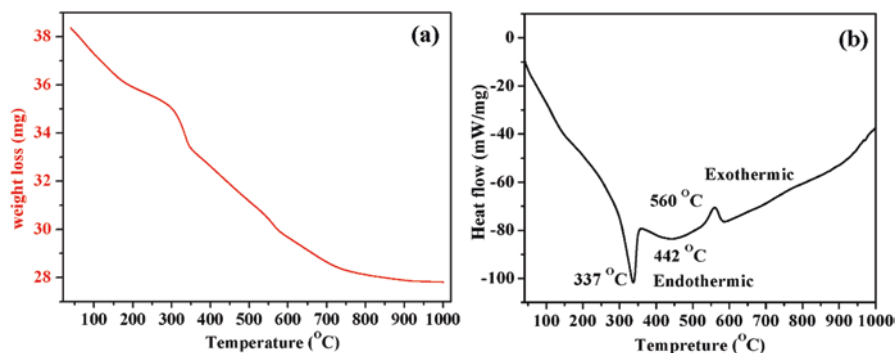

Fig. 22.3 Plots of TGA and DSC curves of FA-Gd_2O_3. (**a**) TGA of folic acid-capped-gadolinium oxide (FA-Gd_2O_3) and (**b**) DSC of folic acid-capped-gadolinium oxide (FA-Gd_2O_3)
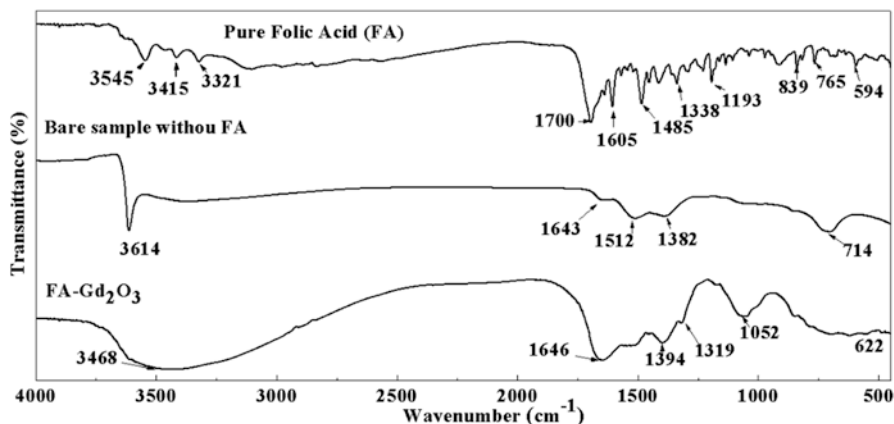
Fig. 22.4 Comparative FTIR spectra of pure folic acid (FA), bare-gadolinium oxide (Gd2O3), and folic acid-capped-gadolinium oxide (FA-Gd_2O_3)

corresponding exothermic peak in DSC plot is at 560 °C [49]. These weight losses are indicative of phase transition and crystallization temperatures of the gadolinium-based samples [50]. The crystallization temperature is supportive to understand the incomplete crystallization as evidenced in XRD analysis where due to lack of crystallization no significant peak intensity is obtained for sample calcinated at 400 °C. The apparent peak at 560 °C associated with named transformation and therefore calcination of gadolinium-based oxide should be carried out at ~600–700 °C or above for perfectly crystalline samples. The surface capping estimated could help in assuming chemical stability and in turn biocompatibility of FA-Gd_2O_3.

4.4   Fourier-Transform Infrared Spectroscopy (FTIR) Analysis

The FTIR (Fig. 22.4) plays a significant role in validating capping analysis showed by UV-vis spectra (Fig. 22.5). Stretching frequencies at ~3545, 3614, and 3468 cm^{-1} are attributed to –O–H stretching vibration of pure FA, bare-Gd_2O_3, and FA-Gd_2O_3, respectively. The peak at ~3415, 3321, and 1605 cm^{-1} corresponds to N–H stretching and vibration, ~1700 cm^{-1} for C=O stretching, ~1485 cm^{-1} for absorption band of phynyl ring, ~1338 cm^{-1} for amide-III of FA, ~1193 cm^{-1} for C–O stretching vibration, and ~800–600 cm^{-1} for C–C stretching for pure FA. The pure FA shows amide I and III vibrational peaks at 1605 and 1338 cm^{-1}, respectively. The peak shifting in this domain can be regarded as conclusive for successful capping of FA over Gd_2O_3 surface. The peak at ~1646 and 1394 cm^{-1} shows shift of ~41 and 56 cm^{-1} inferring successful capping of Gd_2O_3 [26].

4.5   UV-Visible Spectrophotometer and Toxicity Studies through Leaching of Gd³⁺ Ions

4.5   *UV-Visible Spectrophotometer and Toxicity Studies*
through Leaching of Gd³⁺ Ions

The UV-vis spectra of the aqueous dispersion of pure FA and FA-Gd_2O_3 have been compared and presented in Fig. 22.5. The pure FA shows two UV-Vis absorbance at 282 nm and 365 nm for the $n \rightarrow \pi^*$ transitions of C=O bond while $\pi \rightarrow \pi^*$ transition of aromatic C–C ring. The shift in the absorbance spectra of FA-Gd_2O_3 to 276 nm and 362 nm assures conjugation of FA over Gd_2O_3.

   The leaching of Gd³⁺ ions was estimated using xylenol orange dye as indicator and measured by UV-visible spectroscopy. The coordination chemistry of free Ln³⁺ ions with disodium salt of xylenol orange is reported [51]. The Ln³⁺ ions in its free state coordinate with the xylenol orange and deprotonate the complex to change the color of solution from reddish orange to violet and as a result of which the absorption are shifted to higher wavelength [52]. Figure 22.5c shows the spectra of xylenol orange solution in pH 5.8. The varying (increase) concentration of Gd³⁺ ions cause the absorption peak at ca.437.5 nm to decrease its band intensity which is indicated
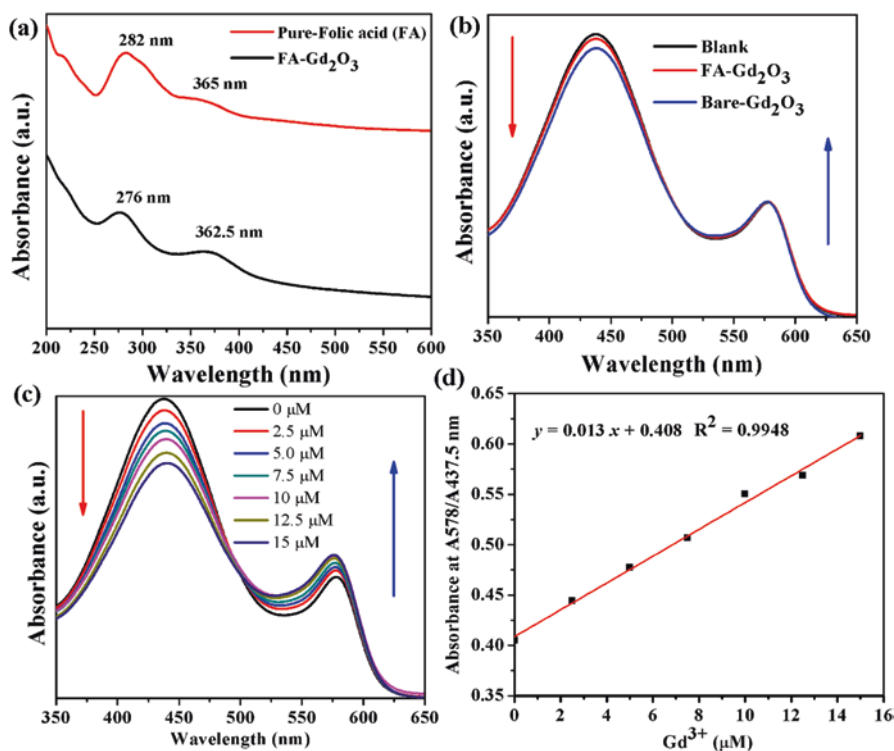

Fig. 22.5 (**a**) Comparative UV-vis spectra of pure folic acid (FA) and folic acid-capped-gadolinium oxide nanorods (FA-Gd_2O_3). (**b**) Spectrophotometric detection of leached Gd³⁺ ions by UV-visible spectroscopy using xylenol orange from bare Gd_2O_3 and FA-Gd_2O_3 and compared with blank. (**c**) Calibration curve obtained by increase in Gd³⁺ ions concentration from 0 to 15 μM (**d**) calibration plot of absorbance (A578/A437.5 nm) versus concentration of Gd³⁺ ions

in graph by red arrow heading downward. Simultaneously the absorption peak at ca.578 nm starts to increase its band intensity demonstrated by blue arrow heading upward. The shift in the observed absorption peaks help in plotting the calibration plot to calculate the unknown concentration in the solution of xylenol orange at pH 5.8. Figure 22.5d shows calibration plot, which is plotted by ratio of absorbance at A578/A437.5 nm versus varying concentration of Gd^{3+} ions in micromolar (μM). As per the fitted equation of calibration plot (Fig. 22.5d), concentration was found to be 1.58 μM and 0.49 μM for bare-Gd_2O_3 and FA-Gd_2O_3, respectively. The calculation using the mentioned concentration demonstrated 0.019% and 0.006% of leached Gd^{3+} ions from bare-Gd_2O_3 and FA-Gd_2O_3 samples, respectively. To validate our data of the leached Gd^{3+} ions as detected using xylenol orange through UV-vis spectroscopy, the leaching study was also performed with ICP-OES. The results from ICP-OES showed no leaching of Gd^{3+} ions in pH 7.4 PBS medium.

4.6 Inductive Coupled Plasma-Optical Emission Spectroscopy Analysis

The inductive coupled plasma-optical emission spectroscopy (ICP-OES) was used for estimation of Gd^{3+} ions composition in bare-Gd_2O_3 (1.33 g L^{-1}) and FA-Gd_2O_3 (1.77 g L^{-1}), respectively. The results are in well agreement with the calculated synthesis precursor's ratios, and therefore synthesis could be tuned by varying precursor's molar ratio to achieve other desired products.

4.7 In Vitro Longitudinal Relaxivity Measurement

The Gd-based samples are MR sensitive, and therefore we tested our samples and compared between bare and FA-capped Gd_2O_3. Literature report suggests the role of confinement of the gadolinium oxide nanoparticles to boost the T_1 contrast ability [53]. It is interesting to note the role of bare and capped Gd_2O_3 used as contrast agent. Therefore, the ability of the bare Gd_2O_3 nanorods and FA-capped Gd_2O_3 nanorods were evaluated. To enhance T_1 contrast of the present samples 1.5 Tesla human scanner (Siemens Essenza 1.5 T) with Inverse Recovery (IR) sequence and setting the parameters TR = 2000 ms for acquiring 30 points with time interval from 500 to 5000 ms, repetition time = 3 were used. The r_1 values for bare Gd_2O_3 nanorods and FA-capped Gd_2O_3 nanorods were 11.57 mM^{-1} s^{-1} and 13.3 mM^{-1} s^{-1}, respectively. This increment in the r_1 value accounted for ~13% increase in r_1 values could be due to sufficient capping to confine the Gd^{3+} ions which may have been loosely bound over the surface of nanoparticles. It is also supported by the previous experiment of Gd^{3+} ions leached from bare nanorods in larger amount, ~3 times than FA-capped Gd_2O_3 nanorods. This leaching in bare samples could have reduced the MR intensity than FA-capped sample. Our results are best supported by the previous reports, where PVP-capped gadolinium oxide spherical particles showed r_1 value of ~10.28 mM^{-1} s^{-1} which could be due to the fact of ligand size of capping as
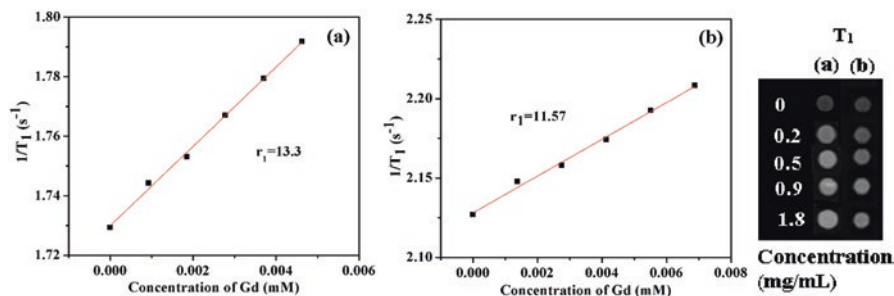
Fig. 22.6 Analysis of relaxation rate R_1 ($1/T_1$) against gadolinium ion concentration for (**a**) FA-GdNRs and (**b**) bare-GdNRs with T_1-weighted MR images

discussed earlier [54, 55]. The value is ~22.7% lower than the present work. Figure 22.6 shows the comparative T_1 images of the bare Gd_2O_3 nanorods, and FA-capped Gd_2O_3 nanorods revealed an enhancement of MR signals with increase in concentration. The T_1 images always starts from dark to gray with the increase in concentration of gadolinium compounds. It is clearly observed from the color of the T_1-weighted phantom images of bare Gd_2O_3 nanorods and FA-capped Gd_2O_3 nanorods, which increases with concentration of the samples.

4.8   Drug Loading and Release

The drug-loading and release profile was performed using 5-FU as model drug. 5-FU is used for colon cancer, cervical cancer, esophageal cancer, pancreatic cancer, stomach cancer, and breast cancer. The drug was dissolved in water at 2 mg/mL concentration (6.28 mmol) and added to ~2.5 mg bare-Gd_2O_3 and FA-Gd_2O_3, respectively. The loading was carried out by incubating the dispersant for 12 h in shaker-incubator at shaking speed of 200 shaking per minute for sufficient loading. The amount of loading was calculated by using supernatant of the centrifuged dispersant mixture of 5-Fu and bare/FA-Gd_2O_3. The obtained absorbance was fitted to its calibration plot equation and later to Eq. 22.2. For calibration curve, solutions of 5-FU in phosphate buffer (1 mM, pH 7.4) from 1 to 19 µg/mL was used which gave a good linear correlation ($R^2 = 0.999$). The supernatant gave the concentration of the remaining drug after loading was completed. The calibration curve and loading amount was estimated from its UV-vis absorbance at characteristic peak of 266 nm. The obtained values were further used for drug loading by the equation:

$$\%\text{Loading} = \frac{\text{Amount of drug in NPs}}{\text{Amount of NPs}} \times 100 \qquad (22.2)$$

The calculated amount was ~9% and ~28% for bare Gd_2O_3 and FA-Gd_2O_3, respectively. The loading efficiency was calculated using theoretical loading from equation:

$$\text{Theoritical loading}(\%) = \frac{\text{Amount of drug added}}{\text{Amount of NPs}} \times 100 \qquad (22.3)$$

The loading efficiency for bare Gd_2O_3 was ~4.5% and ~14% for FA-Gd_2O_3 using the equation as

$$\%\text{Loading efficiency} = \frac{\text{Actual loading}}{\text{Theoritical loading}} \times 100 \qquad (22.4)$$

The drug-loading capacity was found to get enhanced with FA capping. This could be attributed to the increase in surface area and the surface functionalization sites associated with capping molecule. The 5-flurouracil (5-FU) with its simple structure is a low-molecular-weight drug (130.08 Dalton) having size of 3 × 6 Å which could fit well and easily get trapped by high-molecular-weight capping and targeting agent like FA (441.40 Dalton) [56, 57].

The drug release profile for 5-FU-loaded bare Gd_2O_3 and FA-Gd_2O_3 is shown in Fig. 22.7. The drug-loaded particles were re-dispersed in water to fill in dialysis bag

Fig. 22.7 Five-FU release profile of bare-gadolinium oxide (Gd_2O_3) and folic acid-capped-gadolinium oxide (FA-Gd_2O_3)
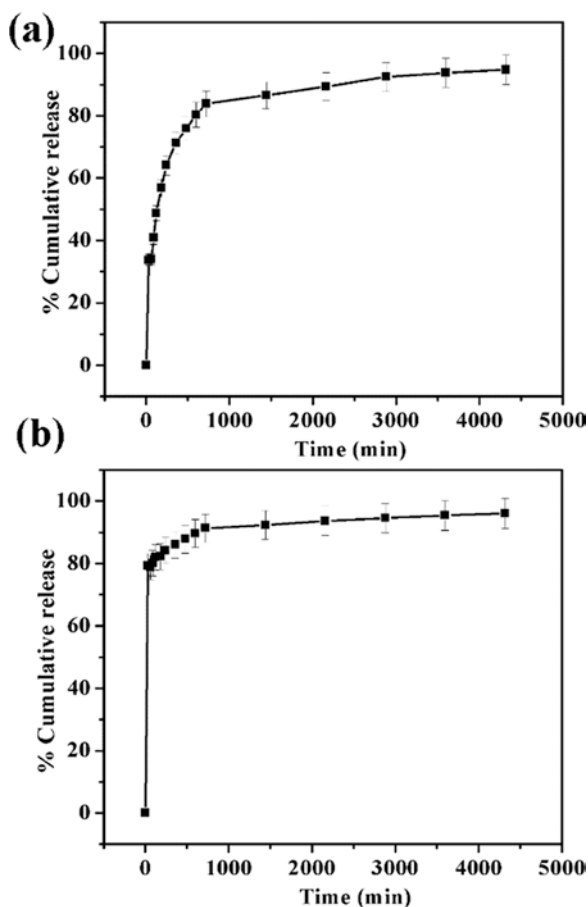
(MWCO 12,000 Daltons) against 30 mL of phosphate-buffered saline (PBS) buffer solution (pH 7.4) in 50 mL centrifuge tube and kept at 100 rpm and 37 °C. The drug release amount was measured by pipetting 2 mL of aqueous releasing buffer medium at mentioned time intervals and scanned by UV-vis spectroscopy. The initial burst release could be due to loosely bound drug molecules to the surface. The cumulative release percentage for bare Gd_2O_3 and FA-Gd_2O_3 was around 94 and 96% in 72 h, respectively. Although the release of drug was higher initially for FA-Gd_2O_3, later, the sustained release was observed. This release profile could be highly beneficial for long-term dose-dependent therapy.

5   Conclusion

The chapter has included the detailed explanation on diverse properties of lanthanide-based materials over their counterparts like transition metals and organic molecules like dyes. It has also highlighted the need of morphology and shape of nanomaterials for biomedical applications. The basic understanding of capping and surface tailoring has been discussed. The best possible mechanism for the elongated anisotropic shape of the lanthanide-based oxide has been discussed thoroughly. The special focus has been made in the transition and crystallizing temperature for the conversion from the hexagonal phase to cubic phase and explained with XRD, TGA, DSC, and FTIR. This detailed analysis has been used for understanding the use of the sample for their application as MRI contrast agent and drug delivery.

References

1. Mattoussi, H., & Rotello, V. M. (2013). Inorganic nanoparticles in drug delivery. *Advanced Drug Delivery Reviews, 65*(5), 605–606.
2. Siegel, R. L., Miller, K. D., & Jemal, A. (2017). Cancer statistics, 2017. *CA: A Cancer Journal for Clinicians, 67*(1), 7–30.
3. Shen, J., Zhao, L., & Han, G. (2013). Lanthanide-doped upconverting luminescent nanoparticle platforms for optical imaging-guided drug delivery and therapy. *Advanced Drug Delivery Reviews, 65*(5), 744–755.
4. Rizvi, S. A. A., & Saleh, A. M. (2018). Applications of nanoparticle systems in drug delivery technology. *Saudi Pharmaceutical Journal, 26*(1), 64–70.
5. Zhang, Y., Wei, W., Das, G. K., & Yang Tan, T. T. (2014). Engineering lanthanide-based materials for nanomedicine. *Journal of Photochemistry and Photobiology C: Photochemistry Reviews, 20*, 71–96.
6. Duan, C., Liang, L., Li, L., Zhang, R., & Xu, Z. P. (2018). Recent progress in upconversion luminescence nanomaterials for biomedical applications. *Journal of Materials Chemistry B, 6*(2), 192–209.
7. Opoku-Damoah, Y., Wang, R., Zhou, J., & Ding, Y. (2016). Versatile nanosystem-based cancer theranostics: Design inspiration and predetermined routing. *Theranostics, 6*(7), 986–1003.
8. Teo, R. D., Termini, J., & Gray, H. B. (2016). Lanthanides: Applications in cancer diagnosis and therapy. *Journal of Medicinal Chemistry, 59*(13), 6012–6024.

9. Ha-Thi, M.-H., Delaire, J. A., Michelet, V., & Leray, I. (2010). Sensitized emission of luminescent lanthanide complexes based on a phosphane oxide derivative. *The Journal of Physical Chemistry-A, 114*(9), 3264–3269.

10. Yang, D., Ma, P., Hou, Z., Cheng, Z., Li, C., & Lin, J. (2015). Current advances in lanthanide ion (Ln^{3+})-based upconversion nanomaterials for drug delivery. *Chemical Society Reviews, 44*(6), 1416–1448.

11. Kwon, O. S., Song, H. S., Conde, J., Kim, H. I., Artzi, N., & Kim, J. H. (2016). Dual-color emissive upconversion nanocapsules for differential cancer bioimaging in vivo. *ACS Nano, 10*(1), 1512–1521.

12. Shan, S.-N., Wang, X.-Y., & Jia, N.-Q. (2011). Synthesis of $NaYF_4$:Yb^{3+}, Er^{3+} upconversion nanoparticles in normal microemulsions. *Nanoscale Research Letters, 6*(1), 539.

13. Chen, G., Qiu, H., Prasad, P. N., & Chen, X. (2014). Upconversion nanoparticles: Design, nanochemistry, and applications in theranostics. *Chemical Reviews, 114*(10), 5161–5214.

14. Gao, W., Dong, J., Yan, X., Liu, L., Liu, J., & Zhang, W. (2017). An further enhancement in red upconversion emission in single $LiYbF_4$:Ho^{3+} microparticle through codoping Ce^{3+} ions. *Journal of Luminescence, 192*, 513–519.

15. Xue, Z., Yi, Z., Li, X., Li, Y., Jiang, M., Liu, H., et al. (2017). Upconversion optical/magnetic resonance imaging-guided small tumor detection and in vivo tri-modal bioimaging based on high-performance luminescent nanorods. *Biomaterials, 115*, 90–103.

16. Li, X., Yi, Z., Xue, Z., Zeng, S., & Liu, H. (2017). Multifunctional $BaYbF_5$:Gd/Er upconversion nanoparticles for in vivo tri-modal upconversion optical, X-ray computed tomography and magnetic resonance imaging. *Materials Science and Engineering-C, 75*, 510–516.

17. Dai, Y., Xiao, H., Liu, J., Yuan, Q., Ma, P., Yang, D., et al. (2013). In vivo multimodality imaging and cancer therapy by near-infrared light-triggered trans-platinum pro-drug-conjugated upconverison nanoparticles. *Journal of the American Chemical Society, 135*(50), 18920–18929.

18. Fedoryshin, L. L., Tavares, A. J., Petryayeva, E., Doughan, S., & Krull, U. J. (2014). Near-infrared-triggered anticancer drug release from upconverting nanoparticles. *ACS Applied Materials & Interfaces, 6*(16), 13600–13606.

19. Chowdhuri, A. R., Laha, D., Pal, S., Karmakar, P., & Sahu, S. K. (2016). One-pot synthesis of folic acid encapsulated upconversion nanoscale metal organic frameworks for targeting, imaging and pH responsive drug release. *Dalton Transactions, 45*(45), 18120–18132.

20. Ma, J., Huang, P., He, M., Pan, L., Zhou, Z., Feng, L., et al. (2012). Folic acid-conjugated LaF_3:Yb,Tm@SiO_2 nanoprobes for targeting dual-modality imaging of upconversion luminescence and X-ray computed tomography. *The Journal of Physical Chemistry-B, 116*(48), 14062–14070.

21. Walker, D. K. (2004). The use of pharmacokinetic and pharmacodynamic data in the assessment of drug safety in early drug development. *British Journal of Clinical Pharmacology, 58*(6), 601–608.

22. Bashir, S., Teo, Y. Y., Naeem, S., Ramesh, S., & Ramesh, K. (2017). Correction: pH responsive *N*-succinyl chitosan/poly (acrylamide-co-acrylic acid) hydrogels and in vitro release of 5-fluorouracil. *PLoS One, 12*(9), e0185505.

23. Toloudi, M., Apostolou, P., & Papasotiriou, I. (2015). Efficacy of 5-FU or oxaliplatin monotherapy over combination therapy in colorectal cancer. *Journal of Cancer Therapy, 6*, 345–355.

24. Rejinold, N. S., Muthunarayanan, M., Chennazhi, K. P., Nair, S. V., & Jayakumar, R. (2011). 5-Fluorouracil loaded fibrinogen nanoparticles for cancer drug delivery applications. *International Journal of Biological Macromolecules, 48*(1), 98–105.

25. Bagheri, A., Arandiyan, H., Boyer, C., & Lim, M. (2016). Lanthanide-doped upconversion nanoparticles: Emerging intelligent light-activated drug delivery systems. *Advancement of Science, 3*(7), 1500437.

26. Xing, P., Chu, X., Ma, M., Li, S., & Hao, A. (2014). Supramolecular gel from folic acid with multiple responsiveness, rapid self-recovery and orthogonal self-assemblies. *Physical Chemistry Chemical Physics, 16*(18), 8346–8359.

27. Sen, G. S., Kuzelka, J., Singh, P., Lewis, W. G., Manchester, M., & Finn, M. G. (2005). Accelerated bioorthogonal conjugation: A practical method for the ligation of diverse functional molecules to a polyvalent virus scaffold. *Bioconjugate Chemistry, 16*(6), 1572–1579.

28. Elnakat, H., & Ratnam, M. (2004). Distribution, functionality and gene regulation of folate receptor isoforms: Implications in targeted therapy. *Advanced Drug Delivery Reviews, 56*(8), 1067–1084.

29. Zhang, X., Ge, J., Xue, Y., Lei, B., Yan, D., Li, N., et al. (2015). Controlled synthesis of ultrathin lanthanide oxide nanosheets and their promising pH-controlled anticancer drug delivery. *Chemistry-A European Journal, 21*(34), 11954–11960.

30. Rogosnitzky, M., & Branch, S. (2016). Gadolinium-based contrast agent toxicity: A review of known and proposed mechanisms. *Biometals, 29*, 365–376.

31. FDA. (2015). *FDA evaluating the risk of brain deposits with repeated use of gadolinium-based contrast agents for magnetic resonance imaging (MRI)*, 7–10.

32. FDA Drug Safety. (2017, May 22). *FDA safety announcement-FDA identifies no harmful effects to date with brain retention of gadolinium-based contrast agents for MRIs: Review to continue*, 2–5.

33. FDA. (2017). *FDA warns that gadolinium-based contrast agents (GBCAs) are retained in the body; requires new class warnings*, 1–4.

34. Cho, M., Sethi, R., Ananta Narayanan, J. S., Lee, S. S., Benoit, D. N., Taheri, N., et al. (2014). Gadolinium oxide nanoplates with high longitudinal relaxivity for magnetic resonance imaging. *Nanoscale, 6*(22), 13637–13645.

35. Ranga, A., Agarwal, Y., & Garg, K. J. (2017). Gadolinium based contrast agents in current practice: Risks of accumulation and toxicity in patients with normal renal function. *Indian Journal of Radiology Imaging, 27*(2), 141–147.

36. Aime, S., & Caravan, P. (2009). Biodistribution of gadolinium-based contrast agents, including gadolinium deposition. *Journal of Magnetic Resonance Imaging, 30*(6), 1259–1267.

37. Wang, J., Li, W., & Zhu, J. (2014). Encapsulation of inorganic nanoparticles into block copolymer micellar aggregates: Strategies and precise localization of nanoparticles. *Polymer, 55*(5), 1079–1096.

38. Kim, C. R., Baeck, J. S., Chang, Y., Bae, J. E., Chae, K. S., & Lee, G. H. (2014). Ligand-size dependent water proton relaxivities in ultrasmall gadolinium oxide nanoparticles and in vivo T_1 MR images in a 1.5 T MR field. *Physical Chemistry Chemical Physics, 16*(37), 19866–19873.

39. Vairapperumal, T., Saraswathy, A., Ramapurath, J. S., Kalarical Janardhanan, S., & Balachandran Unni, N. (2016). Catechin tuned magnetism of Gd-doped orthovanadate through morphology as T_1-T_2 MRI contrast agents. *Scientific Reports, 6*(1), 34976.

40. Tegafaw, T., Xu, W., Lee, S. H., Chae, K. S., Cha, H., Chang, Y., et al. (2016). Ligand-size and ligand-chain hydrophilicity effects on the relaxometric properties of ultrasmall Gd_2O_3 nanoparticles. *AIP Advances, 6*(6), 065114.

41. Cao, Y., Xu, L., Kuang, Y., Xiong, D., & Pei, R. (2017). Gadolinium-based nanoscale MRI contrast agents for tumor imaging. *Journal of Materials Chemistry B, 5*(19), 3431–3461.

42. Ma, X., Zhao, Y., & Liang, X.-J. (2011). Theranostic nanoparticles engineered for clinic and pharmaceutics. *Accounts of Chemical Research, 44*(10), 1114–1122.

43. Hemmer, E., Venkatachalam, N., Hyodo, H., & Soga, K. (2012). The role of pH in PEG-b-PAAc modification of gadolinium oxide nanostructures for biomedical applications. *Advances in Materials Science and Engineering, 2012*, 1–15.

44. Lee, K., Bae, Y., & Byeon, S. (2010). pH Dependent Hydrothermal Synthesis and Photoluminescence of Gd_2O_3:Eu Nanostructures. *Nanowires Science and Technology* Edited by Nicoleta Lupu, https://doi.org/10.5772/39489.

45. Majeed, S., & Shivashankar, S. A. (2014). Rapid, microwave-assisted synthesis of Gd_2O_3 and Eu:Gd_2O_3 nanocrystals: Characterization, magnetic, optical and biological studies. *Journal of Materials Chemistry B, 2*(34), 5585.

46. Mekuria, S. L., Debele, T. A., & Tsai, H. (2017). Encapsulation of gadolinium oxide nanoparticle (Gd_2O_3) contrasting agents in PAMAM Dendrimer templates for enhanced magnetic resonance imaging in vivo. *ACS Applied Materials & Interfaces, 9*(8), 6782–6795.

47. Rocha, L. A., Schiavon, M. A., Ribeiro, S. J. L., Gonçalves, R. R., & Ferrari, J. L. (2015). Eu^{3+}-doped SiO_2–Gd_2O_3 prepared by the sol–gel process: Structural and optical properties. *Journal of Sol-Gel Science and Technology, 76*(2), 260–270.
48. Hazarika, S., & Mohanta, D. (2016). Oriented attachment (OA) mediated characteristic growth of Gd_2O_3 nanorods from nanoparticle seeds. *Journal of Rare Earths, 34*(2), 158–165.
49. Kang, J., Min, B., & Sohn, Y. (2015). Synthesis and characterization of $Gd(OH)_3$ and Gd_2O_3 nanorods. *Ceramics International, 41*(1), 1243–1248.
50. Chaudhary, S., Kumar, S., Umar, A., Singh, J., Rawat, M., & Mehta, S. K. (2017). Europium-doped gadolinium oxide nanoparticles: A potential photoluminescencent probe for highly selective and sensitive detection of Fe^{3+} and Cr^{3+} ions. *Sensors and Actuators B: Chemical, 243*, 579–588.
51. Barge, A., Cravotto, G., Gianolio, E., & Fedeli, F. (2006). How to determine free Gd and free ligand in solution of Gd chelates: A technical note. *Contrast Media & Molecular Imaging, 1*(5), 184–188.
52. Zhang, S., Jiang, Z., Liu, X., Zhou, L., & Peng, W. (2013). Possible gadolinium ions leaching and MR sensitivity over-estimation in mesoporous silica-coated upconversion nanocrystals. *Nanoscale, 5*(17), 8146.
53. Chaudhary, A., Gupta, A., & Nandi, C. K. (2015). Anisotropic gold nanoparticles for the highly sensitive colorimetric detection of glucose in human urine. *RSC Advances, 5*(51), 40849–40855.
54. Xu, W., Miao, X., Oh, I., Chae, K. S., Cha, H., Chang, Y., et al. (2016). Dextran-coated ultrasmall Gd_2O_3 nanoparticles as potential T_1 MRI contrast agent. *ChemistrySelect, 1*(19), 6086–6091.
55. Vahdatkhah, P., Madaah Hosseini, H. R., Khodaei, A., Montazerabadi, A. R., Irajirad, R., Oghabian, M. A., et al. (2015). Rapid microwave-assisted synthesis of PVP-coated ultrasmall gadolinium oxide nanoparticles for magnetic resonance imaging. *Chemical Physics, 453–454*, 35–41.
56. Du, P.-Y., Gu, W., & Liu, X. (2016). A three-dimensional Nd(III)-based metal–organic framework as a smart drug carrier. *New Journal of Chemistry, 40*(11), 9017–9020.
57. Leelakanok, N., Geary, S., & Salem, A. (2018). Fabrication and use of PLGA-based formulations designed for modified release of 5-fluorouracil. *Journal of Pharmaceutical Sciences, 107*(2), 513–528.